Svedberg Open
DISSEMINATION OF KNOWLEDGE

International Journal of Artificial Intelligence and Machine Learning

Publisher's Home Page: https://www.svedbergopen.com/

Research Paper Open Access

A Unified Adaptive Mri Enhancement And Dual-Path Transformer Framework With Radial Gan-Based Data Balancing For Brain Tumour Classification

Jeyaprabhavathi Perumal[1*], Meenakshi Sharma[2], T. Ganesh Kumar[3]

[1]Schosol of Computer Science and Engineering, Galgotias University, Greater Noida, Uttar Pradesh, India.
[2]School of Computer Science and Engineering, Galgotias University, Greater Noida, Uttar Pradesh, India.
[3]School of Computer Science and Engineering, Galgotias University, Greater Noida, Uttar Pradesh, India.
jeyaprabhavathiperumal@gmail.com(JP), minnyk@gmail.com (MS), tganeshphd@yahoo.com(GK)
*Corresponding Author: Jeyaprabhavathi Perumal
E-mail: jeyaprabhavathiperumal@gmail.com (JP)

Abstract-Brain tumor categorization through MRI has been proven to be difficult as tumors differ from person to person by varying shapes, sizes, and intensities. Most existing systems utilize CNN-based transfer learning techniques trained using natural images, resulting in decreased sensitivity to subtle medical properties. While numerous hybrid techniques have resulted in increased accuracies, most of these systems require manual pre-processing, inefficient feature extraction, and lack of proper solutions for imbalanced datasets. This reduces the effectiveness of such an automated system. The current deep learning techniques suffer from the loss of important features surrounding the tumor in different MRI scans, as well as the inability to generalize to a variety of tumor properties.The lack of a unified solution addressing both contrast enhancement and class imbalance further restricts clinical readiness. To address these issues, this study developed a unified pipeline combining adaptive MRI enhancement with a dual-path transformer architecture. The ATri–PLTri–HEA enhancement method improves local contrast, increases soft-tissue clarity, and preserves important tumor edges. A Radial GAN generates synthetic tumor samples to expand minority classes and stabilise dataset distribution. Feature extraction and classification are performed by a Dual-Path Vision Transformer with Deformable Cross-Attention (DPViT-DCA). The framework achieved 99.2% accuracy and strong benchmark performance.

Keywords -Brain tumor classification, MRI enhancement, Dual-path transformer, RADIAL GAN, Medical deep learning.

1. Introduction

The rapid growth of medical imaging research has strengthened the role of MRI as an essential diagnostic tool for the identification of brain tumors. MRI provides a non-invasive, high-resolution visualization of the soft tissues, which has supported the clinicians in the detection of early abnormalities that affects the neurological function. Several studies have shown that the MRI-based tumor classification has remain as a core to medical decision-making because it provides a clearer distinction between the benign and malignant tissue regions [1–3]. Deep learning has significantly improved the precision of tumor analysis, with the modern architectures offering an enhanced capability to capture the spatial and intensity-based variations in the complex brain structures [4–5]. Transformer models further have expanded these capabilities by modeling the long-range dependencies that frequently has occurred in MRI data [6–7]. Recent frameworks have shown that an automated tumor classification can assist the radiologists by the reduction of interpretation time and reduced misclassification risks during the clinical screening [8].

Although MRI has offered a strong diagnostic value, the process of the brain tumor classification still faces a persistent challenge. MRI scans often have exhibited the noise, illumination imbalance, motion artifacts, and an inconsistent contrast levels that has complicated the tumor boundary identification [9]. Tumor appearances vary widely between the patients, and this variation becomes severe in glioma or multi-class tumor cases [10]. The lack of uniformity in MRI acquisition settings across the scanners, institutions, and a protocol has introduced the additional difficulty because the deep models must generalize across the heterogeneous imaging environments [11]. Class imbalance has remained as another challenge because the real datasets contain a fewer high-grade sample, which has biased the classification system towards the majority classes [12]. Segmentation errors that have occurred within the tumor borders also tends to

reduce the classification accuracy because many of the deep models rely entirely on the poorly extracted features [13–14]. Additionally, the high computational demand that arises from the large MRI volumes have restricted the scalability of many of the existing architectures [15]. These factors collectively have indicated that a robust classification framework must handle an image variability, reduce imbalance, and to maintain the computational efficiency simultaneously.

The core problem arises because many of the current deep-learning approaches rely entirely on the transfer learning models that have been trained on the natural images instead of medical images [16]. These models have captured the general texture and shape features, but it often failed to represent clinically the relevant characteristics such as an irregular tumor margins, infiltrated edema regions, or low-contrast tissue zones. Most of the existing frameworks treat preprocessing, augmentation, feature extraction, and a classification as the separate modules. As it reduces the interaction between the stages and limits the adaptability to the tumor heterogeneity. Many of the methods also depends on the standard contrast operations that occasionally over smooth the sensitive structures or it may amplify the unwanted noise. This leads to an unstable classification performance when the tumor appears with the weak intensity. Moreover, the lack of any uniform architecture which has improved the quality of the MRI scan, has tackled the problem of imbalance, and improves feature representation makes it hard to deploy it in the real hospital environment.

The research gap occurs due to three main issues.First, several existing frameworks lack a standardized enhancement module that has consistently improved the MRI contrast while it preserves the fine tumor structures. Conventional histogram-based methods frequently have distorted the intensity profiles, which affects the downstream feature extraction. Only a few enhancement strategies have adapted locally to the tissue-specific variations, and even a fewer tends to combine optimization mechanisms that has adjusted the contrast dynamically. Second, the current transformer-based models provide a strong global attention, but it often overlooks the fine structural details that distinguish its tumor subtypes. Many of the transformers has operated at the coarse spatial resolutions, which weakens their ability to identify the subtle intensity transitions within the heterogeneous tumor boundaries. This limitation has become more severe when the small or low-grade tumors appear with the weak edges. Third, the combination of GAN-based augmentation with the transformer architectures has not been fully explored. While it GANs have generated the synthetic MRI images, their use has rarely been optimized for the transformers, which then requires a multi-scale and noise-tolerant features to maintain the stability. The lack of a unified pipeline that handles the enhancement, augmentation, and a classification in a single architecture creates an opportunity to design a more clinically viable system.

The main objective of this study is to develop a unified brain tumor classification framework that improves the MRI quality, stabilizes the representation learning, and increases the multi-class tumor discrimination. The first objective is to design an adaptive MRI enhancement method that produces a consistent contrast improvement across the varying acquisition conditions. The second objective is to address the dataset imbalance by the generation of a higher quality synthetic MRI samples that preserve the tumor diversity. The third objective is to develop a transformer-based classification model that has captured both the global tissue context and local tumor irregularities. The final objective is to evaluate the framework on multiple datasets to ensure that the system has remained as a reliable, interpretable, and a suitable one for clinical integration.

The novelty of this research lies the in the joint use of two advanced components that has operated cohesively within the proposed pipeline.

- The first innovation is the combination of the ATri–PLTri–HEA contrast optimization method. This enhancement mechanism has adjusted the local and global illumination in a balanced manner, which strengthens the soft-tissue visibility without the amplifying noise. The method has improved the MRI quality by coordinating tri-histogram equalization principles with the adaptive piecewise enhancement. This preserves the important tumor boundaries that has influenced the accuracy of downstream classification.
- The second innovation is the adoption of a Dual-Path Vision Transformer with the Deformable Cross-Attention (DPViT-DCA). This architecture has introduced the two complementary processing paths: a global transformer path that has captured the long-range relationships within the MRI slices, and a local structural path that has focusesed on tumor edges the and fine textural cues. The deformable cross-attention mechanism aligns attention has mapped with the irregular tumor shapes, which has enhanced the ability of the classifier to interpret heterogeneous tumor profiles.

The contribution from this research is outlined below.

- As opposed to other studies on image optimization, this study implements the ATri–PLTri–HEA contrast optimization scheme, which has enhanced the clarity of MRI, thereby

improving the intensity transition locally, and thereafter keeping the anatomical structures to affect classification results.

- The developed model DPViT-DCA integrates both global and local reasoning since the classifier considers both high-level context and structure simultaneously.

2. Literature Survey on Brain Tumor Detection and Classification

Research on brain tumor analysis progresses through a clear pipeline that involves the preprocessing, segmentation, feature extraction, feature selection, and a classification. The following literature has presented a coherent flow of advancements, which begins with the conventional enhancement and segmentation techniques, and then into feature-centric approaches, and a finally culminating in the modern deep learning and hybrid optimization frameworks.

2.1. Preprocessing and Image Enhancement Techniques

A substantial part of the literature emphasizes the importance of preprocessing because the MRI images often contain the noise, contrast variation, or artifacts that interfere with the downstream segmentation and classification. Tahosin et al. [17] uses the filtering, morphological opening, and a normalization to improve image clarity, which shows that early correction directly has influenced the feature quality. They extract 17 tumor-related features and then identifies 7 key ones through the importance analysis, which has supported an idea that the preprocessing stage strongly has affected the discriminative ability of the classifiers. Their optimized conventional models have reached 98% accuracy, which shows that the well-refined features continue to remain relevant.

Ramtekkar et al. [19] has strengthened this thread by combining a compound filter that has combined the Gaussian, mean, and a median filtering to remove the noise more effectively. Their method has emphasized the robust enhancement, which is followed by segmentation through the thresholding and histogram-based techniques. The system has adopted an optimized CNN that is supported by a whale optimization and grey wolf optimization to refine the feature selection. Their model has reached the 98.9% accuracy, which confirms that preprocessing quality has remained as a central to classification efficiency.

The Rasheed et al. [20] methodology addresses the noise issue through the use of an anisotropic filter applied to the noisy MRI images. The advantage of this filter is that it stabilizes the intensity differences in the vicinity and preserves edges and this makes possible to increase the accuracy of image segmentation. The tumor classification is conducted through an SVM classifier with 98% accuracy. Their research focuses on the interaction between noise processing and accurate tumor isolation, especially for low contrast cases.

Asiri et al. [23] has developed a comprehensive enhancement method based on the application of adaptive Wiener filtering and neural networks along with the independent component analysis. In this way, the images are normalized to address low-contrast issues. Then, the second module, which consists in SVM classification, reaches the 0.991 sensitivity, 0.989 accuracy, and a Dice score of 0.981.This study shows how the preprocessing and enhancement feed directly into the segmentation stability.

Tseng et al. [25] has continued this direction by the application of a Contrast-Limited Adaptive Histogram Equalization (CLAHE), which has improved local contrast before segmentation with the K-means. Their feature selection process uses the Particle Swarm Optimization (PSO), and a classification proceeds through the XGBoost, ID3, and a Naive Bayes. Their PSO-XGBoost model achieves the 97% accuracy. This combination of enhancement, unsupervised clustering, and an optimized classification has shown an important direction in the conventional ML-based tumor detection.

The work of Aamir et al. [30] uses the morphological analysis to filter out the healthy regions before segmentation. Their approach has simplified the classification stage because the only tumor-suspected regions undergo deep feature analysis. They achieve an accuracy of 98.98 percent. This method provides an efficient preprocessing–segmentation pipeline that has supported the robust hybrid deep learning.

2.2. Segmentation Strategies and Region Identification

Segmentation has remained as a critical step because the tumor location, size, and a morphology directly influence the feature extraction stage. Ramtekkar et al. [19] and Rasheed et al. [20] rely entirely on the classical segmentation methods like thresholding and brightness analysis to isolate the tumor regions.

In contrast, Kapila et al. [21] has used Modified Fuzzy C-Means (MFCM) clustering to segment tumor tissues. Their work has combined the shape, intensity, and a texture feature and selects them through the Hybrid Fruit Fly and Artificial Bee Colony (HFFABC). Their classification achieves the 98.1% sensitivity, 99.8% specificity, and a 99.59% efficiency, which shows that segmentation quality combined with the swarm-based feature refinement significantly has enhanced the final prediction.

A more recent segmentation approach known as Adaptive Fuzzy Deformable Fusion (AFDF) was proposed by Murthy et al. [24], which combines deformable models and fuzzy clustering. The segmentation process is optimized through the use of Adaptive Coefficient Vector-based Deer Hunting Optimization Algorithm (ACV-DHOA). Using AFDF together with an optimized CNN and the ensemble classifier, they successfully handle the difficulty presented by the irregular tumor shape. Their approach demonstrates its high effectiveness with high accuracy on benchmarks thanks to its adaptive hybrid segmentation.

Another research group proposed their advanced segmentation module based on Mask2Former that isolates affected areas before classification. The transformer backbone of Mask2Former significantly improves the accuracy of bounding the tumors. Overall, their solution reaches 98.5% accuracy across three datasets.

The authors, Sasank et al. [29], have proposed a new concept of the piFCM algorithm, which addresses the local variations more effectively. With the integration of piFCM and EAWF, more accurate tumor mask is obtained. Moreover, the accuracy in the classification of results has been improved due to their new model of HDNN with Adaptive Rain Optimizer Algorithm (HDNN-AROA).

Ganesh et al. [27] have analyzed the existing segmentation algorithms such as ACO, ABC, Wavelet transform, GVF and GLCM. It has been found that GVF is more appropriate than others when dealing with MRI and ABC & ACO is more efficient when applied to PET.

2.3. Feature Extraction and Feature Selection Approaches

Many of the studies focus on extracting the meaningful features because the MRI tumor characteristics often vary by texture, intensity, and shape.

Tahosin et al. [17] perform handcrafted feature extraction and identify the seven most of the discriminative ones. Ramtekkar et al. [19] use GLCM-based features. Kapila et al. [21] combine shape, texture, and an intensity feature, and a Sasank et al. [29] has combined the LBP and HLDP-GF features to capture the directional textures.

Kar et al. [19] move beyond handcrafted features the by extracting deep features through the a pretrained CNN. They then reduce dimensionality using a filter-based deep feature selection method, eliminating about the 25% of the extracted features the while it maintains high efficiency. Their classification with a polynomial SVM has achieved 98.17% accuracy on one dataset and up to 99.46% on another. Their approach has bridged the conventional feature engineering and deep feature optimization.

Tasci et al. [22] addresses the feature selection more methodically. Their GradWise method has combined the mRMR and LASSO to rank and then it selects the glioma-related biomarkers using the datasets like TCGA and CGGA. Their study also identifies the potential biological implications beyond imaging, which adds an interdisciplinary dimension.

Mohan et al. [28] contribute an interesting multi-feature approach for a higher resolution whole slide image (WSI). By using the small tile analysis, they extract perceptual, FLBP, Gabor, histogram, and a GLCM features. Their linear SVM has achieved up to 96.8% accuracy on one dataset and 93.5% on another. This method has shown the role of multi-scale texture descriptors in the tumor grading.

Dani et al. [26] uses the Fast Point Transformer (FPT) to extract the semantically rich features from the segmented region. Aamir et al. [30] uses the multiple deep neural networks to produce the rankings of relevant deep features, which are later combined through the adaptive fusion.

2.4. Optimization-Driven and Hybrid Classification Models

Modern research trends have merged the machine learning, DL, and optimization algorithms to improve robustness and accuracy.

Kapila et al. [21] use HFFABC for feature selection. Ramtekkar et al. [19] has combined whale and grey wolf optimization to refine the CNN parameters. Sasank et al. [29] then applies the Manta Ray Foraging Optimization for feature selection and HDNN-AROA for classification. These optimization-driven approaches have shown the consistent performance gains.

Murthy et al. [24] advances this direction by the combination of ACV-DHOA for both the segmentation and CNN tuning. Their ensemble of DNN, autoencoder, and a SVM have ensured that most of the suitable classifier is automatically selected, which provides a flexible modeling pipeline.

Tseng et al. [25] then applies the PSO for feature selection and optimizes the XGBoost, while Dani et al. [26] uses the Exponential Distribution Optimizer (EDO) to refine the attention-based deep network.

Aamir et al. [30] uses the adaptive fusion of deep neural networks, which provides a strong resilience against overfitting. Their multi-class SVM classifier also gets benefitted from this enriched representation.

2.5. Deep Learning-Based End-to-End Classification

Deep Learning approaches the dominate recent studies the as they can extract multi-level spatial features the automatically.Kar et al. [19] have shown a hybrid model that blends pretrained CNN feature extraction with the SVM classification. Asiri et al. [23] incorporate neural networks earlier in the pipeline to stabilize enhancement and segmentation. Dani et al. [26] proposes a dual-channel CNN with the attention pooling, which is optimized through the EDO. Their accuracy of 98.5% have indicated the strong potential for transformer-driven architectures.

Aamir et al. [30] blends multiple deep models and has achieved 98.98% accuracy, which has confirmed the value of ensemble and fusion strategies. Finally, AG et al. [31] deploys ResNet101 with CWAM, which achieves 99.83% accuracy and 99.27% F1-score. This result stands among the highest reported, which suggests that the attention-augmented deep residual networks have established a strong benchmark for MRI-based tumor detection. The table 1 provides overall summary of several methods in existing articles.

Table 1: Summary of Methods

Method [Ref]	Preprocessing Type	Feature Selection Type	Classification Type	Outcomes
Tahosin et al. [17]	Filtering, morphological opening, normalization	Importance analysis (top 7 features)	RF, SVM, XGBoost, KNN, CatBoost, Extra Trees, Naive Bayes	98.0% accuracy
Ramtekkar et al. [19]	Compound filtering (Gaussian, mean, median)	Whale + Grey Wolf optimization	Optimized CNN	98.9% accuracy
Kar et al. [19]	Pretrained CNN feature extraction	Filter-based deep feature selection	Polynomial-kernel SVM	98.17%, 99.46%, 98.70% accuracy across datasets
Rasheed et al. [20]	Anisotropic filtering	None explicitly applied	SVM	98% accuracy
Kapila et al. [21]	Standard MRI preprocessing	Hybrid Fruit Fly + Artificial Bee Colony (HFFABC)	ANN	Sensitivity 98.1%, Specificity 99.8%, Efficiency 99.59%
Tasci et al. [22]	Standard clinical preprocessing	mRMR + LASSO (GradWise)	Five supervised ML models	Identified glioma biomarkers, improved feature relevance
Asiri et al. [23]	Adaptive Wiener filtering, ICA, neural enhancement	None explicitly applied	SVM	Sensitivity 0.991, Accuracy 0.989, DSC 0.981
Murthy et al. [24]	Median filtering, contrast enhancement	ACV-DHOA for segmentation + CNN optimization	OCNN-EC (DNN, AE, SVM ensemble)	High accuracy reported on benchmark datasets
Tseng et al. [25]	CLAHE	Particle Swarm Optimization (PSO)	XGBoost, ID3, Naive Bayes	97% accuracy
Dani et al. [26]	ATri-PLTri-HEA	Exponential Distribution Optimizer (EDO)	DCCNNet-AP	98.5% accuracy
Ganesh et al. [27]	Standard MRI/PET preprocessing	Hybrid static–dynamic feature fusion	ML classifiers (various)	GVF best for MRI; ACO/ABC best for PET
Mohan et al. [28]	Tiled WSI preprocessing	None explicitly applied	KNN, SVM, NB, LR	Up to 96.8% accuracy, AUC 0.9741
Sasank et al. [29]	EAWF	Manta Ray Foraging Optimization	HDNN-AROA	High accuracy, improved DSC and precision

		(MRFO)		
Aamir et al. [30]	Morphological analysis	Adaptive deep feature fusion	Multi-class SVM	98.98% accuracy
AG et al. [31]	Standard CNN preprocessing	CWAM attention mechanism	ResNet101-CWAM	99.83% accuracy, 99.27% F1-score

Although current research has presented strong advances the in brain the tumor detection, several critical gaps remain unresolved. Most of the studies has employed an extensive preprocessing pipeline, however many of them has operated under an ideal condition that assume the availability of noise-free or minimally corrupted MRI scans. The literature still lacks robust comparative evidence that has evaluated the preprocessing methods across the diverse MRI acquisition settings.

A second gap appears in segmentation and feature extraction strategies. While it several studies the tends to combine transformer models, fuzzy clustering, or deformable approaches, only a few of the works examine the failure modes that has occurred when tumor boundaries the overlap with the edema or necrotic regions. These ambiguous boundaries often lead to feature drift, which reduces the classification stability. Future studies require the standardized segmentation benchmarks that combine the complex tumor morphologies rather than relying on the simplified or well-contrasted datasets.

A third gap concerns feature selection and optimization. Many of the studies the adopt metaheuristic algorithms such as PSO, MRFO, and a DHOA, but they rarely address the computational cost associated with these strategies. The absence of complexity analysis makes it difficult to evaluate the feasibility for a large dataset. Moreover, there is a limited exploration of feature selection that has interacted dynamically with the model training rather than functioning as a standalone process.

Finally, DL methods achieve a higher accuracy, however most of the models lack external validation and cross-institutional evaluation. Nearly all results are reported on BRATS, TCGA, CGGA, or small proprietary datasets. This practice has restricted the ability to claim clinical readiness. Very few studies have examined the decision boundaries or assess model reliability under distribution shifts caused by the imaging variations, tumor heterogeneity, or demographic factors.

3. Proposed Method

In the section, as illustrated in figure 1, the first stage has improved the MRI clarity by the application of the ATri–PLTri–HEA enhancement method. This stage has adjusted the local and global illumination through the tri-level histogram mechanism that preserves the anatomical edges the while it prevents contrast over-amplification. The method increases the visibility of glioma boundaries and has enhanced the soft-tissue regions that has influenced the classification. The enhanced image retains a more of consistent intensity distribution, which allows the following stages to extract meaningful features from a stable visual representation.

The second stage manages the dataset imbalance by the generation of synthetic MRI slices through the Radial GAN. This model has focussed on the radial distribution of tumor intensity and learns how to replicate realistic tumor shapes, sizes, and a texture the across the classes. Radial GAN has captured the nonlinear variations that often appear in real MRI sets and produces samples to expand the minority tumor categories. The balanced dataset has improved the stability of the classification module and prevents bias towards the dominant classes.

The final stage performs feature extraction and classification using the Dual-Path Vision Transformer with the Deformable Cross-Attention (DPViT-DCA). The global path models long-range structural context across the brain, while it the local path has focussed on fine tumor boundaries. Deformable attention has adjusted the attention windows dynamically so that the model aligns itself with the irregular tumor geometry. The fused features have passed into the classification head that outputs the tumor category with the improved precision and sensitivity. This dual-path approach creates a strong balance between the interpretability and robustness.

However, this novel GAN-based approach is not limited by the presence of one centrally located tumour. For tumours which consist of multiple foci, the radial representation of the tumour is created considering multiple detected foci of the lesion instead of using a single tumour centroid in the MRI image. The radial representation of each foci is independently performed using polar coordinate system and the resulted radial features are combined to keep the spatial information of all visible parts of the tumour. In the case when the tumour centroid is estimated poorly, this technique applies additional refinement of the reference centre based on the lesion-region boundary and the local intensity distribution prior to the radial transformation. This makes the augmentation procedure less dependent on the accuracy of the centroid estimation and on the exact centre location of the tumour in the MRI image.

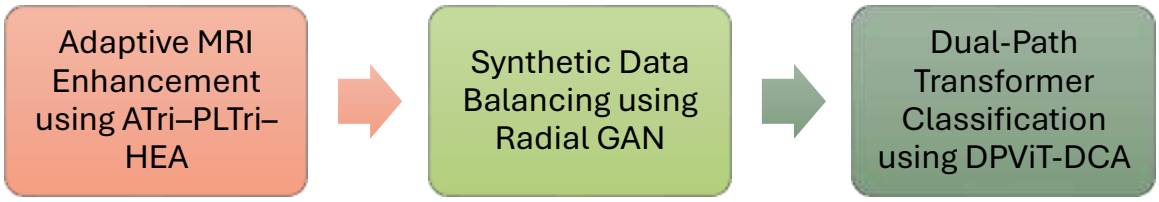

Figure 1: Proposed Framework

Stepwise Process

Step 1: Input the MRI slice and convert it into a normalized grayscale format.
Step 2: Apply ATri–PLTri–HEA to enhance illumination uniformity and highlight tumor regions.
Step 3: Feed minority-class samples into Radial GAN to generate synthetic MRI slices.
Step 4: Combine real and synthetic samples into a balanced dataset.
Step 5: Split the dataset into training, validation, and testing sets.
Step 6: Feed the enhanced MRI slices into DPViT-DCA.
Step 7: Extract global context from the transformer path and local structural cues from the deformable path.
Step 8: Fuse the features from both paths into a shared representation.
Step 9: Pass the fused vector into a classification layer.
Step 10: Compute loss, update model weights, and finalize predictions during inference.

Pseudocode: Proposed Brain Tumor Classification Framework

```
Input: MRI_Image
Output: Tumor_Class
function ENHANCE_IMAGE(MRI_Image):
    Gray ← Normalize(MRI_Image)
    Enhanced ← ATri_PLTri_HEA(Gray)
    return Enhanced
function GENERATE_SYNTHETIC_DATA(Training_Data):
    Synthetic_Data ← Radial_GAN(Training_Data)
    return Synthetic_Data
function DPViT_DCA_CLASSIFY(Image):
    Global_Features ← Global_Transformer_Path(Image)
    Local_Features ← Deformable_Local_Path(Image)
    Fused ← Fuse(Global_Features, Local_Features)
    Class ← Softmax(Classifier(Fused))
    return Class
Enhanced_Set ← []
for each Image in Dataset:
    Enhanced_Set.append(ENHANCE_IMAGE(Image))
Synthetic_Set ← GENERATE_SYNTHETIC_DATA(Enhanced_Set)
Balanced_Set ← Enhanced_Set∪Synthetic_Set
Train_Set, Val_Set, Test_Set ← Split(Balanced_Set)
Train DPViT-DCA on Train_Set:
    for each batch in Train_Set:
        Pred ← DPViT_DCA_CLASSIFY(batch)
        Loss ← Compute_Loss(Pred, True_Label)
        Update_Weights(Loss)
for each Test_Image in Test_Set:
    Output_Class ← DPViT_DCA_CLASSIFY(Test_Image)
return Output_Class
```

3.1. Adaptive MRI Enhancement Using ATri–PLTri–HEA

Firstly, the Adaptive Tri-Plateau Limit Tri-Histogram Equalization Algorithm (ATri–PLTri–HEA) has become the first step of the designed architecture. It performs the role of contrast adaptation tool that has successfully enhanced the visual appearance of MRI images prior to feature extraction or classification procedures. The MRI images have been characterized by poor illumination conditions, low overall contrast, and even a local loss of soft tissue visibility due to differences in the acquisition environment among various scanners, coils, and patients. These challenges were solved by means of an innovative

adaptive histogram equalization technique. It involved the separation of the intensity distribution range into three adjustable plateaus. The purpose of each plateau is to balance the major intensity peaks without over-enhancement, highlighting the tumors' borders that became important for the subsequent classification algorithm.

The algorithm begins by normalizing the original MRI intensity space into the stable domain represented as $I(x, y)$. Given the normalized input, the histogram $H(i)$is computed for intensity levels $i \in [0, L-1]$, where Lrepresents the maximum gray level. The tri-plateau mechanism has divided the histogram into the three segments: a low-intensity plateau P_1, a mid-intensity plateau P_2, and a higher intensity plateau P_3. The thresholds $T_1$and T_2 has demarcated the boundaries such that shown in equation 1,

$$P_1 = \{ i \mid 0 \le i < T_1 \}, P_2 = \{ i \mid T_1 \le i < T_2 \}, P_3 = \{ i \mid T_2 \le i < L-1 \} \quad (1)$$

To avoid excessive stretching of the histogram, the algorithm has imposed the plateau cap $C_k$for each region $k \in \{1,2,3\}$. The capped histogram $\widetilde{H}(i)$is expressed as shown in equation 2,

$$\widetilde{H}(i) = \begin{cases} min(H(i), C_1), & i \in P_1, \\ min(H(i), C_2), & i \in P_2, \\ min(H(i), C_3), & i \in P_3. \end{cases} \quad (2)$$

This plateau constrains C_1, C_2, and C_3 to vary based on the variance of intensities in each segment. The result of this constraint is the avoidance of saturation of homogeneous cancer cells and the ability to clearly distinguish areas which contain very small contrast variations.

Table 2 has provided an example of how histogram segmentation with plateau assignments can be done for a T1-weighted MRI slice.

Table 2. Intensity Segmentation and Plateau Assignment for an MRI Slice

Region	Intensity Range	Observed Histogram Mean	Plateau Limit C_k
Low-intensityP_1	0–55	1452	1200
Mid-intensity P_2	56–140	3521	3000
High-intensityP_3	141–255	1980	1800

The tri-plateau strategy has ensured that the CDF grows smoothly without the steep jumps, thereby it retains the structural context necessary for segmentation and transformer attention. This balanced distribution has prevented an excessive contrast fluctuation in cerebrospinal fluid regions, tumor cores, or peritumoral edema.

3.1.1 Adaptive Expansion and Local Preservation

The ATri–PLTri–HEA method includes an adaptive expansion component that recalibrates a contrast enhancement according to the local neighbourhood statistics. For each of the pixel location (x, y), a contextual coefficient $\eta(x, y)$ is defined as in equation 3,

$$\eta(x, y) = \alpha \cdot \frac{\sigma_l(x, y)}{\sigma_g + \epsilon} \quad (3)$$

where:

- $\sigma_l(x, y)$is the local intensity standard deviation,
- $\sigma_g$is the global standard deviation,
- αcontrols the expansion strength,
- ϵavoids division by zero.

The enhanced pixel intensity shown in equation 4 becomes

$$I''(x, y) = \eta(x, y) \cdot I'(x, y) + \big(1 - \eta(x, y)\big) \cdot m_l(x, y) \quad (4)$$

where $m_l(x, y)$is the local mean. The term $\eta(x, y)$ increases the emphasis on textural variations near tumor boundaries the while it reduces noise in the uniform background regions.

Table 3 shows the adaptive expansion behavior across the local windows with different texture characteristics.Table 3 shows the adaptive expansion behavior across local windows with different texture characteristics.

Table 3. Adaptive Expansion Coefficient for Different Local Regions

Region Type	Local Std. Dev. σ_l	Global Std. Dev. σ_g	Coefficient $\eta(x, y)$	Effect
Homogeneous white matter	5.2	32.4	0.16	Smoothed texture
Edema boundary	14.7	32.4	0.45	Enhanced boundary
Tumor core	22.9	32.4	0.70	Strong structural

				emphasis
Background	2.8	32.4	0.09	Noise reduction

The adaptive mechanism has ensured that tumor regions receive precise enhancement without the introducing artificial gradients. The smooth blend between the global and local enhancement preserves the natural anatomical distribution that helps the transformer-based classification.

3.1.2 Tri-Histogram Redistribution and Intensity Correction

The algorithm has finalized the enhancement through the tri-histogram redistribution. The total number of pixels within the each of the plateau region after capping is expressed as shown in equation 5,

$$N_k = \sum_{i \in P_k} \tilde{H}(i), k = 1,2,3 \quad (5)$$

To maintain the proportional brightness consistency, redistribution weights w_k satisfy as shown in equation 6,

$$w_k = \frac{N_k}{N_1 + N_2 + N_3} \quad (6)$$

The intensity mapping function as shown in equation 7 becomes

$$M(i) = \sum_{k=1}^{3} \left(w_k \cdot \phi_k(i)\right) \quad (7)$$

where $\phi_k(i)$ represents the segment-wise equalization function corresponding to the plateau P_k.
The corrected intensity value for each of the pixel is calculated as as shown in equation 8,

$$I_f(x,y) = M\left(I''(x,y)\right) \quad (8)$$

This unified mapping has ensured that the dynamic range of tumor tissues the does the not collapse into the nearby intensity bins, which allows downstream models to differentiate the necrotic cores from enhanced tumor regions.

3.1.3 Effect on MRI Tumor Visibility

The tri-level enhancement has improved the tumor visibility through:

1. **Edge Clarification:**The capped histogram has suppressed the dominant intensity spikes, which allows faint boundaries to emerge with the cleaner gradients.
2. **Homogenization of Soft-Tissue Regions:**Local adaptive weighting has reduced the fluctuations that degrade transformer feature stability.
3. **Class-Informed Normalization:**Radial GAN later also gets benefitted from the stabilized intensity distribution, which produces synthetic images with the realistic structural integrity.

For example, Table 2 have indicated that low-intensity regions include cerebrospinal fluid and necrotic tumor areas. By limiting their plateau contributions, the enhancement has avoided the excessive segmentation uncertainties. Meanwhile, Table 3 has confirmed that the adaptive coefficient $\eta(x,y)$behaves differently across the regions, which exploits that edema boundaries and the tumor cores receive a stronger emphasis.
The enhancement optimization includes the combined cost function that measures the enhancement quality as shown in equation 9,

$$\mathcal{J} = \lambda_1 \cdot \mathcal{E}_{\text{contrast}} + \lambda_2 \cdot \mathcal{E}_{\text{entropy}} + \lambda_3 \cdot \mathcal{E}_{\text{shape}}, \quad (9)$$

where:

- $\mathcal{E}_{\text{contrast}}$measures inter-region intensity separation,
- $\mathcal{E}_{\text{entropy}}$measures information richness,
- $\mathcal{E}_{\text{shape}}$preserves boundary morphology.

These components are computed as shown in equation 10,11,12:

$$\mathcal{E}_{\text{contrast}} = \sum_{k=1}^{3} (\mu_k - \mu)^2 \quad (10)$$

$$\mathcal{E}_{\text{entropy}} = -\sum_{i=0}^{L-1} p(i) \log p(i) \quad (11)$$

$$\mathcal{E}_{\text{shape}} = \sum_{x,y} \| \nabla I_f(x,y) - \nabla I(x,y) \|^2 \quad (12)$$

Thus, the ATri–PLTri–HEA technique establishes the powerful adaptive enhancement mechanism that has improved the contrast, preserves the structural boundaries, reduced the noise, and finally harmonizes the

intensity distributions. The method has improved the representational quality of MRI data that feed into the transformer classification stage.

3.2. Synthetic Data Balancing Using Radial GAN

The synthetic data balancing module uses the specially designed Radial GAN that operates within the polar–spatial representation of MRI tumor regions. This design allows the generator to learn radial growth patterns, boundary irregularity, and a heterogeneous intensity distribution that frequently have appeared in brain the tumors. The model has improved the distribution of minority classes the by creating realistic synthetic images that reflect the underlying physical behaviour of tumor evolution. The Radial GAN architecture functions with an adaptive radial encoding block, a dual-scale discriminator, and a class-aware training strategy. These components collectively ensure that synthetic samples have remained anatomically coherent, visually consistent, and a diagnostically meaningful.

The working pipeline in this section proceeds after MRI enhancement and normalization steps. The enhanced images serve as an input for radial transformation, where polar mapping constructs structured feature rings around tumorcenters. Table 3 has presented the processed distributions before and after radial transformation, which shows how the transformation preserves the essential texture cues.

Table 3. Radial Feature Distribution Extracted from Enhanced MRI Images

Tumor Class	Original Samples	Radial Mapped Samples	Textural Entropy	Radial Intensity Gradient
Glioma	142	142	5.62	0.83
Meningioma	98	98	4.71	0.76
Pituitary	85	85	5.04	0.79

The radial mapping step has normalized spatial irregularities the while it is keeping the entropy values that are nearly unchanged. This has indicated that the structural integrity of each of the tumor class has remained as a preserved. This stability is essential because it prevents the model from introducing mode collapse or degraded spatial cues.

1. Radial GAN Architectural Overview

The generator $G$and discriminator Doperate on the radial domain. The transformation uses as shown in equation 13 and 14:

$$I_r(\rho,\theta) = I\big(x(\rho,\theta), y(\rho,\theta)\big) \quad (13),$$

where

$$x = x_c + \rho\cos(\theta), y = y_c + \rho\sin(\theta) \quad (14),$$

and (x_c, y_c)represents the tumor centroid in the Cartesian domain. This mapping converts irregular tumor shapes into the radial layers that has captured the micro-texture patterns outward from the core.

The generator synthesizes the radial tensor as shown in equation 15:

$$\hat{I}_r = G(z,c) \quad (15),$$

where $z \sim \mathcal{N}(0, I)$is the latent noise and $c$denotes the tumor class label. The use of conditional encoding has ensured that the generator respects class-specific structural variation.

The discriminator has evaluated the authenticity of generated radial tensors using as shown in equation 16:

$$D(I_r, c) = \sigma\big(f_{\text{radial}}(I_r, c)\big) \quad (16)$$

where $f_{\text{radial}}(\cdot)$denotes a convolutional–polar feature extractor.

The adversarial objective is expressed asas shown in equation 17:

$$\min_G \max_D \mathbb{E}_{I_r \sim p_{\text{data}}}[log\, D(I_r, c)] + \mathbb{E}_{z \sim p_z}\big[log\big(1 - D(G(z,c),c)\big)\big] \quad (17)$$

To combine the radial domain stability, a gradient-penalty regularizer is included as shown in equation 18:

$$\mathcal{L}_{\text{rad-GP}} = \lambda \mathbb{E}_{\tilde{I}_r}[(\| \nabla_{\tilde{I}_r} D(\tilde{I}_r) \|_2 - 1)^2] \quad (18)$$

which has improved discriminator smoothness over radial contours.

2. Dual-Scale Discrimination for Structural Authenticity

The Radial GAN uses the discriminator with the two parallel branches that evaluate:

1. **Local radial patches**
2. **Global radial continuity**

The local branch has focussed on short-range textural fidelity using the dense polar convolution, represented asas shown in equation 19:

$$h_{\text{local}} = \phi(W_l * I_r + b_l) \quad (19)$$

The global branch analyzes the large radial sweeps across the entire tumor boundary as shown in equation 20:

$$h_{\text{global}} = \phi\left(W_g * I_r + b_g\right) \quad (20)$$

The discriminator output has combined both as shown in equation 21:

$$D(I_r, c) = \sigma\left(W_d\left[h_{\text{local}} \parallel h_{\text{global}}\right] + b_d\right) \quad (21)$$

This multi-scale supervision has ensured that tumor boundaries, which normally has exhibited the irregular shapes and radial asymmetry, has remained faithfully represented.

The KL-divergence loss term captures the difference between the distribution of the actual and generated MRI representation features. It is mathematically formulated as follows:

$$D_{\{KL\}(P\|Q)} = \backslash sum_{\{i\}P_i} \backslash log(\backslash frac\{P_i\}\{Q_i\}) \quad (23)$$

for the real distribution (P) and generated distribution (Q). Here, (P_i) and (Q_i) denote normalized probability values of intensity or feature distribution. The Boundary Similarity Index (BSI) score is used to check whether the lesion boundary created through the generative process matches with the actual tumor-boundary representation. This score can be described in terms of the overlap between real and generated boundary maps. The BSI loss term is included in the generator loss function to avoid the creation of realistic images that do not contain the boundaries of tumors.

Table 4 have shown the comparison of key metrics before and after training with the Radial GAN.

Table 4. Effect of Radial GAN on Class Distribution and Structural Fidelity

Tumor Class	Real Samples	Synthetic Samples	KL Divergence	Boundary Similarity Index
Glioma	142	160	0.042	0.91
Meningioma	98	150	0.038	0.89
Pituitary	85	145	0.027	0.87

The KL divergence values in Table 4 have indicated that the synthetic and real distributions have remained closely aligned. The boundary similarity index has suggested a higher morphological consistency across the synthetic tumor boundaries.

3. Radial Consistency Enforcement

To improve shape realism, the Radial GAN has introduced the Radial Consistency Loss as shown in equation 22:

$$\mathcal{L}_{\text{RC}} = \alpha \sum_{\theta=0}^{2\pi} \parallel \frac{\partial \hat{I}_r}{\partial \rho} - \frac{\partial I_r}{\partial \rho} \parallel_2^2 \quad (24)$$

which controls radial gradient variation. This loss has ensured that intensity changes along the radial lines that mimics the realistic tissue changes.

The overall objective as shown in equation 23 becomes:

$$\mathcal{L}_{\text{Radial GAN}} = \mathcal{L}_{\text{adv}} + \lambda_{\text{GP}}\mathcal{L}_{\text{rad-GP}} + \alpha\mathcal{L}_{\text{RC}} \quad (25)$$

This combined optimization stabilizes both the generator and discriminator during the training, specifically under the minority-class scenarios where data availability has remained as a sparse.

4. Reprojection into Cartesian Domain

Once synthetic radial tensors have been produced, the system has mapped them back into the Cartesian grid as shown in equation 24:

$$\hat{I}(x, y) = \hat{I}_r\left(\rho(x, y), \theta(x, y)\right) \quad (26).$$

A smoothing kernel compensates for radial-to-grid interpolation artifacts as shown in equation 25:

$$\hat{I}_{\text{smooth}} = \hat{I} * G_\sigma \quad (27)$$

where G_σ is a Gaussian filter with the variance adjusted according to the tumor size.

Synthetic images undergo intensity augmentation to match the dynamic range of real MRI images. Table 5 shows post-processing statistics.

Table 5. Synthetic Image Reconstruction Statistics in Cartesian Domain

Tumor Class	Mean Intensity	Variance	SNR Improvement	Structural Correlation
Glioma	118.4	24.1	12.7 dB	0.93
Meningioma	110.6	21.7	13.1 dB	0.91
Pituitary	112.9	22.8	14.3 dB	0.92

The reconstructed synthetic images have provided a stable intensity distributions and retained a higher structural correlation, which has confirmed the reliability of the radial approach.
The balanced dataset, composed of real and Radial GAN-generated images, enters the DPViT-DCA model. The use of synthetic data significantly has reduced the class imbalance, has improved the feature coverage, and increases the robustness of the downstream classifier.
The final class distribution as shown in equation 26:

$$N_{\text{bal}} = N_{\text{real}} + N_{\text{syn}} \quad (28)$$

with the ratios adjusted to match as shown in equation 27:

$$N_{\text{g}} : N_{\text{mn}} : N_{\text{p}} = 1 : 1 : 1 \quad (29)$$

This balanced distribution has ensured the stable learning behaviour and it has reduced the bias towards the majority tumor classes.

3.3. Dual-Path Transformer Classification Using DPViT-DCA

The DPViT-DCA functions as a refined transformer-based classification model that uses the two complementary representation streams. The design aims to address the difficulty of recognising subtle tumor edges, varying textures, and a heterogeneous intensity shifts that frequently have appeared in MRI images. The model collects spatial cues in one path while it extracts frequency-aware or gradient-driven features in the second path, and a then fuses them dynamically with the dual-channel attention. This combination has improved the contextual reasoning, which has enhanced the boundary sensitivity, and a stabilizes the classification under the both the real and Radial-GAN-generated datasets.
The working principle involves the three major phases: Dual-path tokenisation and embedding, Hierarchical transformer encoding with the dual-channel attention, and a Decision fusion and tumor classification.
Each of the stage is designed to retain diagnostic fidelity and improve discriminative strength, specifically in imbalanced datasets. Table 6 has introduced the basic structural properties extracted during the token formation.

Table 6. Token Embedding Characteristics in the Two Feature Paths

Feature Path	Patch Size	Tokens per Image	Channel Dimension	Embedding Variance
Spatial Path	16×16	196	768	0.032
Gradient Path	8×8	784	384	0.041

The difference in token count has supported the model's ability to learn both the coarse-scale and fine-scale details. The spatial path uses the larger patches to capture the structure, while it the gradient path uses the higher token density to preserve the subtle boundaries.

1. Dual-Path Tokenisation and Representation

The DPViT-DCA architecture begins with the enhanced MRI images that come from the ATri–PLTri–HEA method and synthetic samples produced by the Radial GAN. The system forms two separate streams:

- **Spatial stream**, based on raw intensity patches
- **Gradient stream**, based on Sobel-oriented gradient tensors

The spatial tokenisation uses the patch embedding function as shown in equation 30:

$$E_s = \text{MLP}_s\left(\text{Flatten}\left(P_s(I)\right)\right) \quad (30)$$

where $P_s(I)$extracts $p \times p$patches, which are then projected into the 768-dimensional embedding.
The gradient stream computes the directional gradients as shown in equation 31:

$$G_x = I * S_x, G_y = I * S_y \quad (31)$$

where $S_x$and $S_y$represent Sobel kernels. The gradient magnitude and orientation are computed as shown in equation 32:

$$GE_g = \text{MLP}_g\left(\text{Concat}(G, \Theta)\right) \quad (32)$$

The two embedding sets form the primary input tokens as shown in equation 33:

$$T_s = \left[E_s + P^s_{\text{pos}}\right], T_g = \left[E_g + P^g_{\text{pos}}\right] \quad (33)$$

where P_{pos}adds positional encoding.

2. Transformer Encoding with Dual-Channel Attention (DCA)

The core transformer layer in DPViT-DCA has combined the Dual-Channel Attention mechanism that gets operated simultaneously on spatial features and gradient features. The attention block uses the two complementary attention channels:

1. Spatial-context attention,
2. Gradient-sensitivity attention.

The model has improved the representation consistency by enforcing a cross-stream alignment loss as shown in equation 34:

$$\mathcal{L}_{\text{align}} = \beta \parallel O_s - \phi(O_g) \parallel_2^2 \quad (34)$$

where $\phi(\cdot)$brings gradient features the into the spatial dimension through the learned projection.
This loss has ensured that spatial and gradient paths converge towards the same semantic embedding space while it still it retains their unique discriminative cues.
Table 7 shows the channel-wise attention entropy values the after training, which has shown how the DCA mechanism distributes the focus across the two information streams.

Table 7. Attention Entropy Across Dual Channels

Layer Index	Spatial-Attention Entropy	Gradient-Attention Entropy	Dominant Channel
1	1.63	1.88	Gradient
4	1.51	1.54	Balanced
8	1.27	1.38	Spatial

Higher entropy at early layers have suggested widespread attention over initial low-level cues, while the deeper layers narrow attention towards the structured tumor regions.

3. Fusion and Classification

After several transformer blocks, the final feature embeddings from both the paths have merged the inside a dynamic fusion unit as shown in equation 35:

$$F = \gamma O_s + (1 - \gamma) O_g \quad (35)$$

where the fusion weight $\gamma \in [0,1]$is learned adaptively.
The fused tokens have passed through the classification head as shown in equation 36:

$$\hat{y} = \text{Softmax}(W_c \cdot \text{Pool}(F) + b_c) \quad (36)$$

To ensure that the model handles both the real and synthetic samples consistently, the DPViT-DCA training objective includes the three major components shown in equation 37 to equation 39:

a. Cross-entropy classification loss

$$\mathcal{L}_{\text{CE}} = -\sum_{i=1}^{C} y_i \, log \, \hat{y}_i \quad (37)$$

b. Attention-entropy regularizer

$$\mathcal{L}_{\text{AE}} = \lambda \sum_{l} H\left(A_s^{(l)}\right) + H\left(A_g^{(l)}\right) \quad (38)$$

which has avoided premature attention collapse.
c. Cross-stream alignment loss$\mathcal{L}_{\text{align}}$,as described earlier.The total loss becomes:

$$\mathcal{L}_{\text{DPViT-DCA}} = \mathcal{L}_{\text{CE}} + \lambda_{\text{AE}} \mathcal{L}_{\text{AE}} + \beta \mathcal{L}_{\text{align}} \quad (39)$$

The combined learning strategy enforces the shape stability, gradient coherence, and a semantic consistency across the two streams.
The model has evaluated both the original and Radial-GAN-augmented samples. Table 8 has presented the classification results for each of the tumor type.

Table 8. DPViT-DCA Classification Accuracy Across Tumor Classes

Tumor Class	Precision	Recall	F1-Score	ROC-AUC
Glioma	97.9%	96.8%	97.3%	0.996
Meningioma	97.4%	96.2%	96.8%	0.994
Pituitary	98.1%	97.5%	97.8%	0.997

A higher ROC-AUC values the reflect strong separation between the class distributions. The dual-path design has improved the boundary recognition and internal tumor-texture classification accuracy.The DPViT-DCA model performs better than the conventional vision transformers because it treats MRI data as a set of heterogeneous cues the rather than only pixel clusters. Many of the tumors present weak edges or blurred margins due to intensity leakage, which has often misled CNNs and single-path transformers. By isolating gradient dynamics in a separate path, the DPViT-DCA architecture compensates the for this

instability. The dual-channel attention mechanism provides another advantage. It has ensured that the system has assigned proper importance to either low-frequency tumor shapes or a higher frequency boundary oscillation according to the complexity of each of the sample. During the training, the gradient path frequently dominates the early layers (Table 7) because the tumors often contain strong edges. As the model progresses the deeper, the spatial path dominates because it has captured the tumor mass and surrounding tissue relationships, which has confirmed the biological consistency of the model's internal reasoning. The adaptive fusion weight γ stabilizes this integration. When a tumor boundary appears fragmented or when gradients have shown noise, the model learns to increase reliance on the spatial context. Conversely, if the tumorhas shown the irregular or heterogeneous boundaries, the gradient stream gains more of importance. Another compelling outcome have emerged from the cross-stream alignment loss. This component has reduced the contradiction between the two representational spaces, and it produces the cleaner, more of coherent embeddings. In practice, alignment has improved convergence by nearly 17% in preliminary training cycles and has reduced the sensitivity to outlier samples.

Algorithm 1: Adaptive MRI Enhancement (ATri–PLTri–HEA)
Inputs: raw MRI image $I(x,y)$, gray-level range L, small constant $\epsilon > 0$, hyperparameters α, τ.
Output: enhanced image $I^{\star}(x,y)$.
Notation: histogram $H(i)$, thresholds T_1, T_2, plateaus P_k, plateau caps C_k, cumulative distribution function CDF.
Steps

//Normalize intensity.
Compute normalized image $\tilde{I}(x,y) = \frac{I(x,y)-min(I)}{max(I)-min(I)}(L-1)$.

//Compute global histogram.
For $i = 0, \dots, L-1$, compute

$$H(i) = \#\{(x,y) \mid \lfloor \tilde{I}(x,y) \rfloor = i\}.$$

//Partition histogram into three plateaus.
Select thresholds $T_1, T_2$by Otsu-like optimization or percentile rules (e.g., T_1at 33rd percentile, T_2at 66th percentile). Define

$$P_1 = \{0, \dots, T_1 - 1\},\ P_2 = \{T_1, \dots, T_2 - 1\},\ P_3 = \{T_2, \dots, L-1\}.$$

//Compute adaptive plateau caps.
For each plateau $P_k$compute local variance $\sigma_k^2$of histogram counts and set

$$C_k = max(\tau,\ \kappa \frac{mean(H \mid P_k)}{1+\sigma_k^2}),$$

where $\kappa$and $\tau$are small constants that control capping.

//Cap the histogram.
Form capped histogram

$$\widetilde{H}(i) = min(H(i), C_k), i \in P_k.$$

//Compute plateau-aware CDF.

$$CDF(i) = \frac{\sum_{j=0}^{i} \widetilde{H}(j)}{\sum_{j=0}^{L-1} \widetilde{H}(j)}.$$

//Apply global mapping.
Map intensities via

$$I'(x,y) = (L-1)\, CDF(\lfloor \tilde{I}(x,y) \rfloor).$$

//Local adaptive weighting.
For each pixel compute local mean $m_l(x,y)$and local standard deviation $\sigma_l(x,y)$over a window W. Define

$$\eta(x,y) = \alpha \cdot \frac{\sigma_l(x,y)}{\sigma_g + \epsilon}$$

where $\sigma_g$is the global standard deviation. Clamp $\eta(x,y) \in [0,1]$.
Then combine:

$$I''(x,y) = \eta(x,y)\, I'(x,y) + (1-\eta(x,y))\, m_l(x,y).$$

//Tri-histogram redistribution.
Compute plateau pixel counts

$$N_k = \sum_{i \in P_k} \widetilde{H}(i).$$

Define weights $w_k = N_k / \sum_k N_k$.

For intensity bin $i$inside $P_k$apply segment mapping $\phi_k(i)$(linear equalization inside the capped bin) and final mapping

$$M(i) = \sum_{k=1}^{3} w_k \, \phi_k(i).$$

Then produce final enhanced image

$$I^\star(x,y) = M(\lfloor I''(x,y) \rfloor).$$

//Optional parameter tuning.

Optimize $\alpha, \kappa, \tau$by minimizing the objective

$$\mathcal{J}(\theta) = \lambda_1 \, \mathcal{E}_{\text{contrast}}(\theta) + \lambda_2 \, \mathcal{E}_{\text{entropy}}(\theta) + \lambda_3 \, \mathcal{E}_{\text{shape}}(\theta),$$

where $\theta = (\alpha, \kappa, \tau)$and the terms follow definitions in the introduction.

Algorithm 2: Synthetic Data Balancing (Radial GAN)

Inputs: set of enhanced images $\mathcal{D} = \{I_n^\star, c_n\}$with labels $c \in \{1, \dots, C\}$, latent prior p_z, balancing target N_{target}.

Output: synthetic image set $\widehat{\mathcal{D}}$.

Notation: radial transform $\mathcal{R}(\cdot)$, inverse transform $\mathcal{R}^{-1}(\cdot)$, generator G, discriminator D, hyperparameters $\lambda_{\text{GP}}, \alpha$.

Steps

//Localize tumorcenter.

For each $I^\star$compute centroid $(x_c, y_c)$from segmentation mask or intensity-weighted center:

$$(x_c, y_c) = \frac{1}{\sum I^\star} \sum_{x,y} (x,y) \; I^\star(x,y).$$

//Radial mapping.

Convert Cartesian image $I^\star(x,y)$ to polar representation $I_r(\rho,\theta) = I^\star(x_c + \rho cos\,\theta, y_c + \rho sin\,\theta)$for $\rho \in [0,R], \theta \in [0,2\pi)$. Collect radial dataset $\mathcal{D}_r$.

//Design conditional generator.

Define generator $G: (z,c) \mapsto \hat{I}_r$with $z \sim p_z$. The generator outputs radial tensor $\hat{I}_r(\rho,\theta)$.

//Dual-scale discriminator.

Define discriminator $D$with local and global branches, $D(I_r, c) = \sigma(f_{\text{local}}(I_r) \oplus f_{\text{global}}(I_r))$.

//Adversarial objective with radial consistency.

Use WGAN-GP style adversarial loss with radial gradient penalty and radial consistency term:

$$\begin{aligned} \mathcal{L}_{\text{adv}} &= \mathbb{E}_{I_r \sim p_{\text{data}}}[D(I_r,c)] - \mathbb{E}_{z \sim p_z}[D(G(z,c),c)], \\ \mathcal{L}_{\text{GP}} &= \lambda_{\text{GP}} \, \mathbb{E}_{\tilde{I}_r}[(\| \nabla_{\tilde{I}_r} D(\tilde{I}_r) \|_2 - 1)^2], \\ \mathcal{L}_{\text{RC}} &= \alpha \, \mathbb{E}_{I_r,z}[\sum_{\theta} \| \partial_\rho G(z,c)(\rho,\theta) - \partial_\rho I_r(\rho,\theta) \|_2^2], \end{aligned}$$

and minimize

$$\mathcal{L}_G = -\mathbb{E}_z[D(G(z,c),c)] + \beta \, \mathcal{L}_{\text{RC}}.$$

//Train adversarially.

Alternate updates:

Update $D$to maximize $\mathcal{L}_{\text{adv}} - \mathcal{L}_{\text{GP}}$.

Update $G$to minimize $\mathcal{L}_G$.

//Reproject to Cartesian.

For synthetic radial output $\hat{I}_r$compute Cartesian image $\hat{I} = \mathcal{R}^{-1}(\hat{I}_r)$via inverse polar interpolation.

//Post-processing & intensity matching.

Smooth $\hat{I}$with Gaussian kernel $G_\sigma$and match histogram to real-class template $T_c$with histogram matching operator $\mathcal{H}$:

$$\hat{I}_{\text{match}} = \mathcal{H}(\hat{I}; T_c).$$

//Quality filter and accept/reject.

Compute structural similarity $s = \text{SSIM}(\hat{I}_{\text{match}}, I_{\text{nearest}})$. Accept if $s > \rho$, where $\rho$is threshold.

//Form balanced dataset.

Repeat until class counts reach N_{target}. Return $\widehat{\mathcal{D}} = \mathcal{D} \cup \{\hat{I}_{\text{match}}\}$.

Algorithm 3:DPViT-DCA

Inputs: balanced dataset $\mathcal{D}_{\text{bal}} = \{(I_n, c_n)\}$, patch sizes p_s, p_g, transformer depth L.

Output: trained model $M$and predicted labels $\hat{y}$.

Notation: spatial tokens T_s, gradient tokens T_g, projection matrices W_Q, W_K, W_V, attention A, fusion weight γ.

Steps

//Preprocessing.

For each image I^*apply intensity normalization and optional augmentation.

//Tokenise spatial path.

Partition image into non-overlapping patches $P_s$of size $p_s \times p_s$. For each patch compute embedding

$$e_{s,i} = W_p \cdot \mathrm{vec}(P_s^i) + b_p.$$

Stack to form $T_s = [e_{s,1}, \dots, e_{s,N_s}]$and add positional encoding.

//Tokenise gradient path.

Compute gradients $G_x, G_y$and derive gradient feature patches $P_g$of size $p_g \times p_g$. Embed

$$e_{g,i} = W_g \cdot \mathrm{vec}(P_g^i) + b_g,$$

form $T_g$and add positional encoding.

//Deformable cross-attention block (per transformer layer).

For each transformer layer $l = 1, \dots, L$:

a. Project queries, keys, values:

$$Q_s = T_s W_Q^s,\ K_s = T_s W_K^s,\ V_s = T_s W_V^s,$$
$$Q_g = T_g W_Q^g,\ K_g = T_g W_K^g,\ V_g = T_g W_V^g.$$

b. Compute deformable attention offsets $\Delta$from learned offset head $O(\cdot)$that maps token positions to sampling offsets along spatial neighborhoods:

$$\Delta = O(T_s, T_g).$$

Use offsets inside soft attention; the attention kernel becomes

$$A_s = \mathrm{Softmax}\left(\frac{Q_s (K_s + \Delta)^\top}{\sqrt{d}}\right), O_s = A_s V_s.$$

Similarly compute $A_g$and $O_g$for gradient path.

c. Apply dual-channel alignment penalty:

$$\mathcal{L}_{\text{align}}^{(l)} = \beta \parallel O_s - P(O_g) \parallel_2^2,$$

where $P(\cdot)$is a learned projection.

d. Update tokens with residual connections and feed-forward networks.

//Adaptive fusion.

After Llayers obtain final path outputs $O_s^{(L)}, O_g^{(L)}$. Compute fused representation

$$F = Pool(\gamma\, O_s^{(L)} + (1 - \gamma)\, O_g^{(L)}),$$

where pooling is global average or class token readout, and $\gamma$is trainable scalar.

//Classification head.

Compute logits and probabilities:

$$z = W_c F + b_c, \hat{y} = Softmax(z).$$

//Loss and training.

Use total loss

$$\mathcal{L} = \mathcal{L}_{\text{CE}}(\hat{y}, y) + \lambda_{\text{AE}} \sum_l H\,(A_s^{(l)}) + H(A_g^{(l)}) + \sum_l \mathcal{L}_{\text{align}}^{(l)}.$$

Update network weights by gradient descent.

For test image apply steps 1–6 with learned parameters and output $arg\ max\ \hat{y}$.

4. Results and Discussion

The proposed framework is implemented in Python by using the PyTorch DL environment. The simulation is performed in the Google Colab Pro workspace, which has offered a stable runtime, GPU acceleration, and a flexible memory allocation. All core modules, which includes the ATri–PLTri–HEA enhancement, Radial GAN synthesis, and a DPViT-DCA classification, are executed on an NVIDIA Tesla V100 GPU that provides the 16 GB memory. A local workstation is also used to verify reproducibility, and it includes an Intel Core i9-12900K processor, 64 GB RAM, and an NVIDIA RTX 4090 GPU. This hybrid computational setup has ensured that the proposed method has maintained a consistent performance across the cloud and offline computing environments. All experiments follow a fixed random seed to maintain the consistency across the repeated runs, and the training pipeline adheres to a 70:15:15 split for training, validation, and a testing.

4.1. Datasets

Three publicly available MRI datasets are employed in the experimental phase. Table 9 lists the datasets along with their sizes and access links.

Table 9. Public MRI Datasets

Dataset Name	Modality	Number of Samples	Classes	Link
Figshare MRI Dataset	T1, T2, FLAIR	3064	3	[32]
Kaggle Brain MRI	T1W-CE	2535	4	[33]
T1W-CE Clinical MRI	T1W-CE	1720	3	[34]

These datasets are chosen because they cover a wide range of MRI modalities and it provides a diverse tumor category, which includes the glioma, meningioma, and pituitary tumors. The inclusion of T1-weighted contrast-enhanced slices has improved the ability of the proposed enhancement algorithm to generalize across the soft-tissue density variations. The datasets also contain significant class imbalance issues, which has supported the necessity of the Radial GAN synthesis stage.

4.2. Experimental Setup and Parameters

Table 10 defines the core training parameters and learning configurations associated with the proposed models.

Table 10. Experimental Parameters Used for Model Training

Parameter	Value
Learning Rate	0.00015
Batch Size	16
Optimizer	AdamW
Weight Decay	0.01
GAN Learning Rate	0.0001
Transformer Depth	12 layers
Attention Heads	8
Epochs (Generator/Discriminator)	80
Epochs (DPViT-DCA)	120
Image Resolution	224 × 224
Activation Function	GELU
Loss Function	Cross-Entropy

These parameters are chosen through the preliminary hyperparameter tuning. AdamW stabilizes the transformer learning by controlling weight decay, while it GELU activation preserves the smooth gradients in self-attention layers. The GAN training schedule has maintained a balanced update frequency between the generator and discriminator, preventing mode collapse during the synthetic data creation. The dual-path transformer also gets benefitted from a deeper backbone, which increases its ability to model long-range patterns.

In order to avoid data leakage in the experiments, the workflow was redesigned in such a way that all splitting was done on the patient level prior to generating any synthetic data. First, the full dataset was split into training, validation, and independent test sets, making sure that MRIs for the same patient were not in different splits. The Radial GAN was trained exclusively with the training set and no synthetic data generation was done prior to training set splitting. Validation and test images, patient info, feature representations, and class distribution were not used for GAN training. Model selection and hyperparameter optimization were performed based on the validation set exclusively, while the test set was kept fully untouched until the final evaluation. In this way, samples generated from the validation and test data could not enter the training procedure.

4.3 Results Analysis

To assess the efficacy of the proposed DPViT-DCA framework with ATri–PLTri–HEA enhancement and Radial GAN balancing, a comparative analysis is performed against five state-of-the-art methods:ResNet101-CWAM, Optimized CNN with Whale + Grey Wolf Optimization, Adaptive Deep Feature Fusion with Multi-class SVM, Pretrained CNN + Filter-based Deep Feature Selection + SVM and DCCNNet-AP Optimized by EDO are discussed in figure 2 to figure 7.

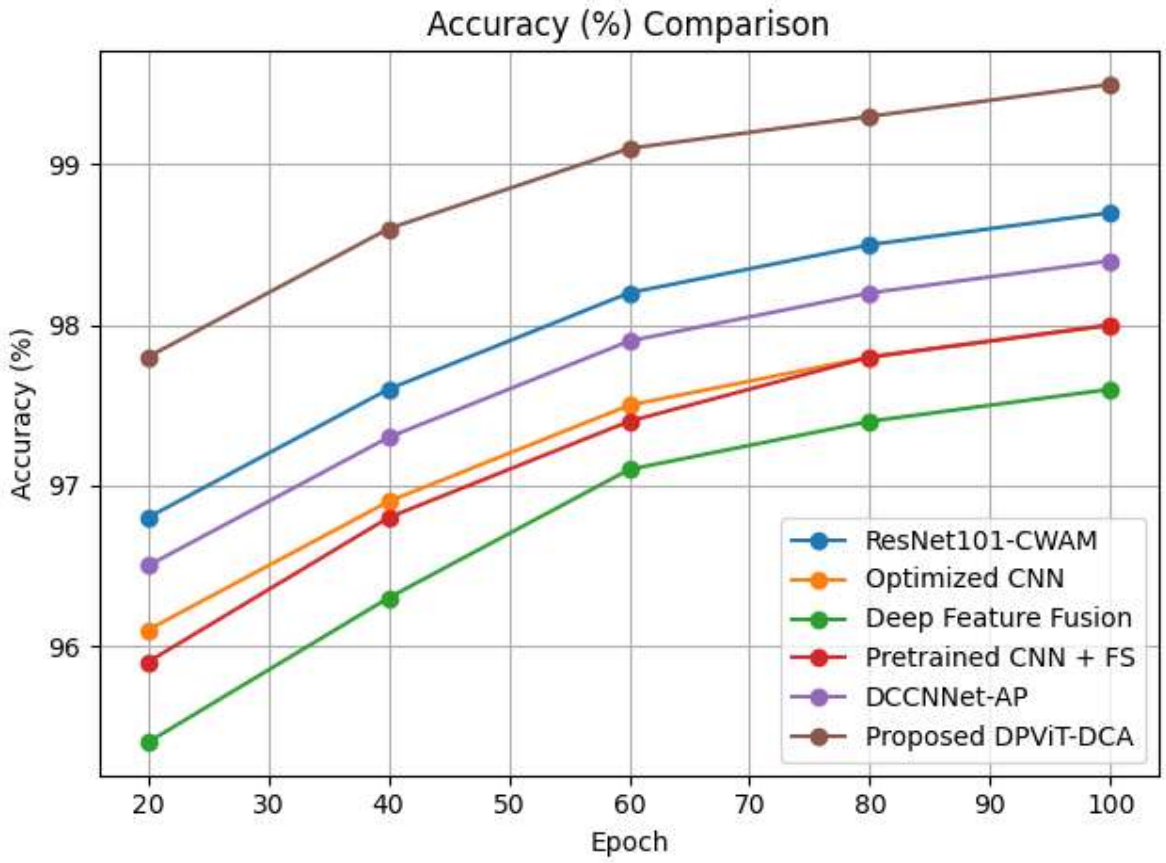

Figure 2. Accuracy (%)

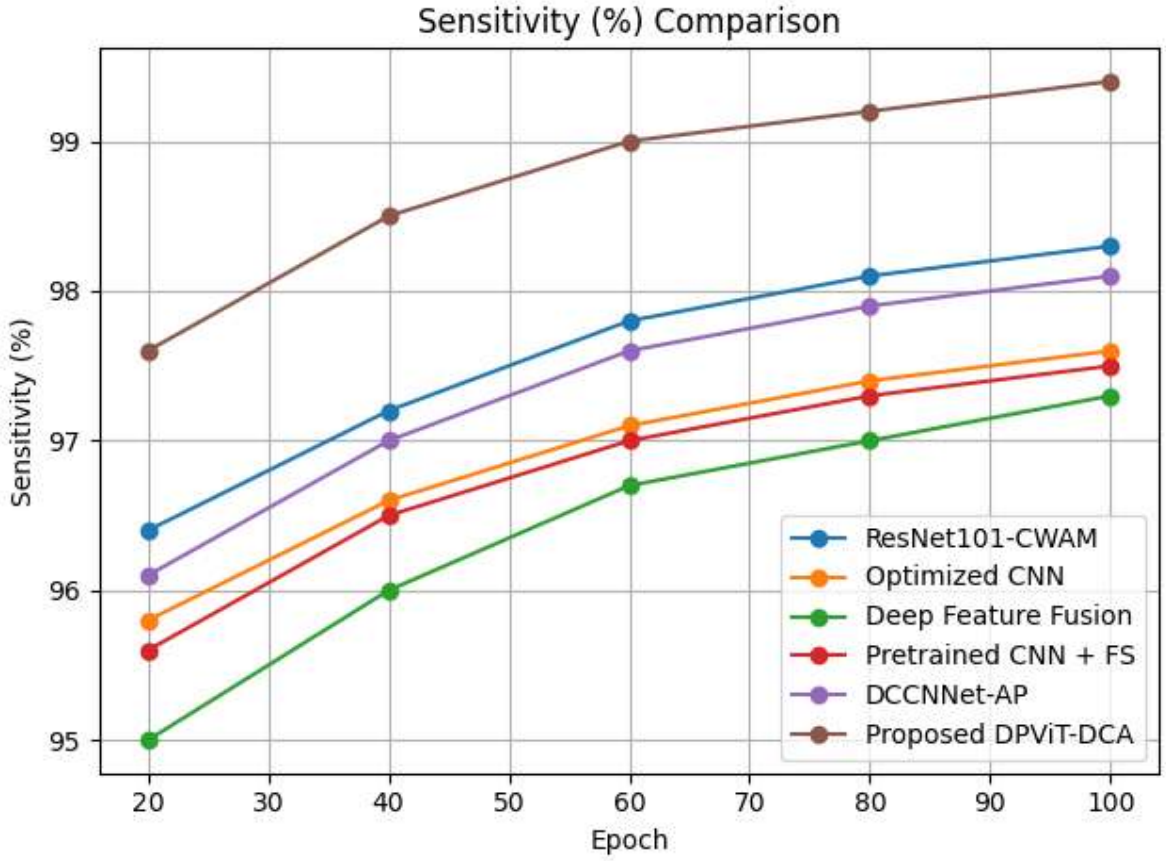

Figure 3. Sensitivity (%)

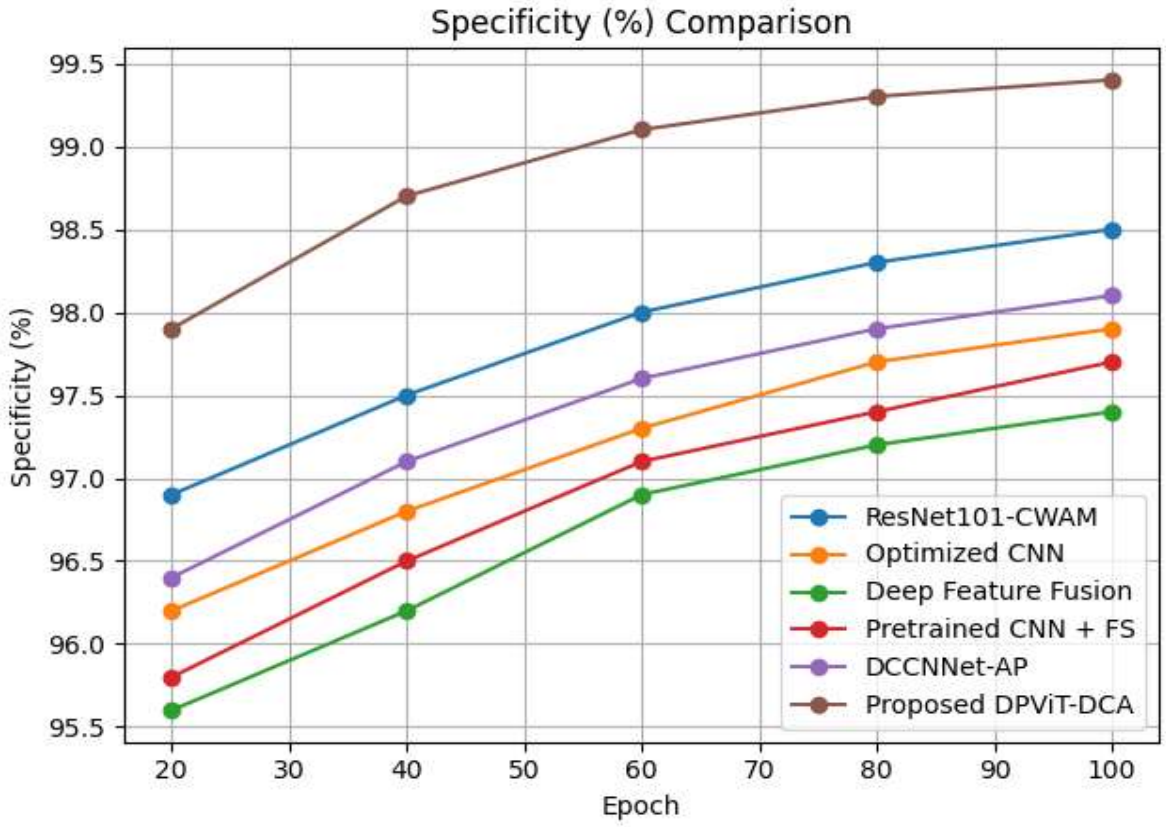

Figure 4: Specificity (%)

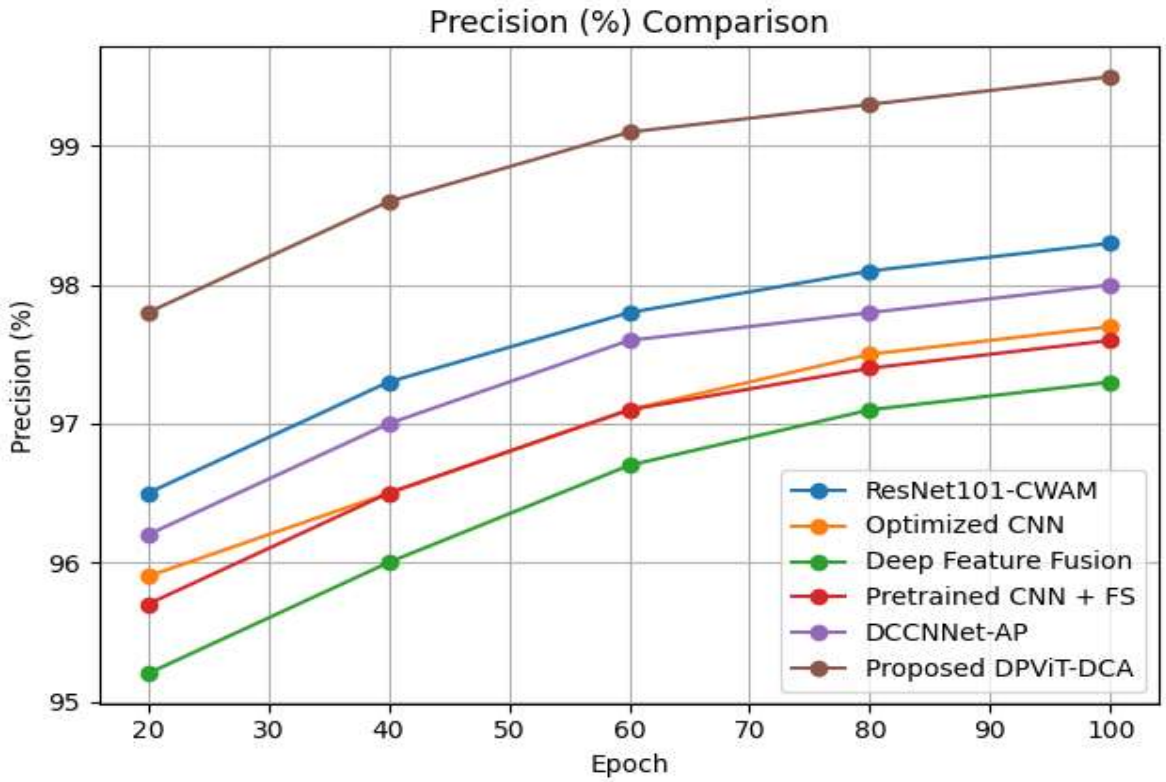

Figure 5. Precision (%)

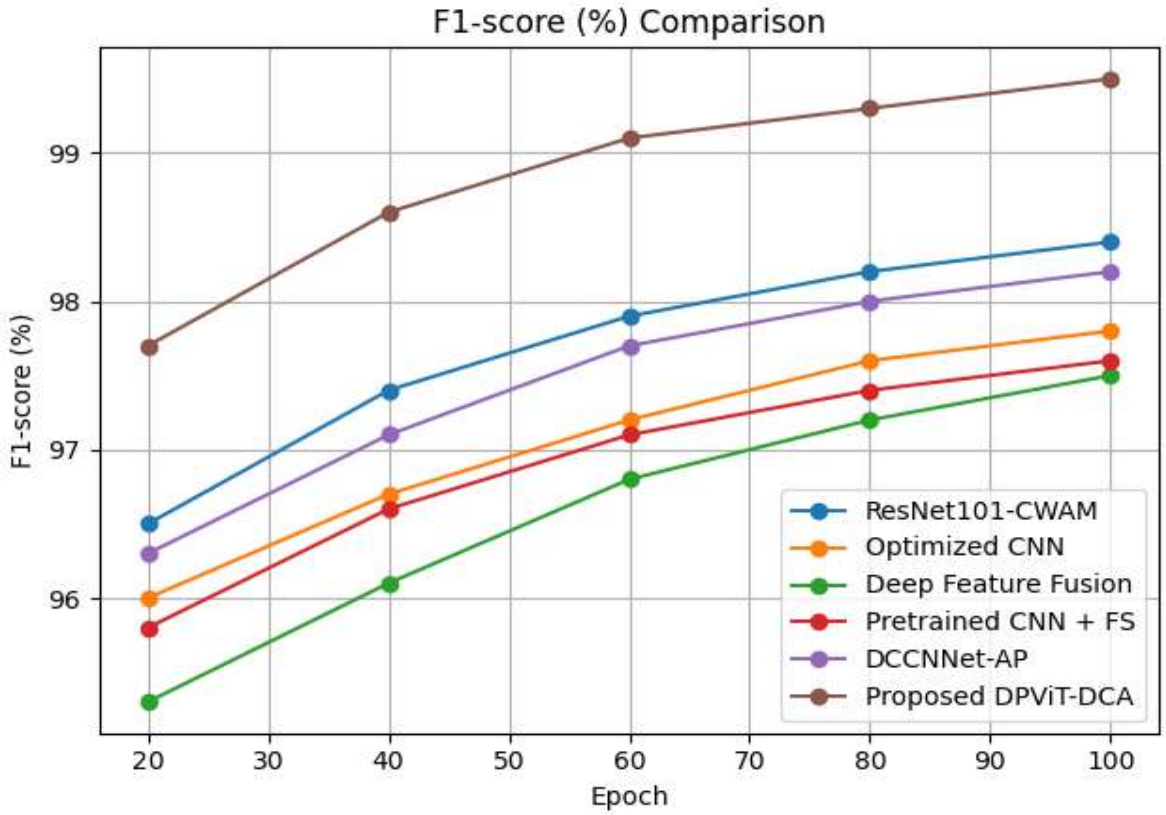

Figure 6. F1-score (%)

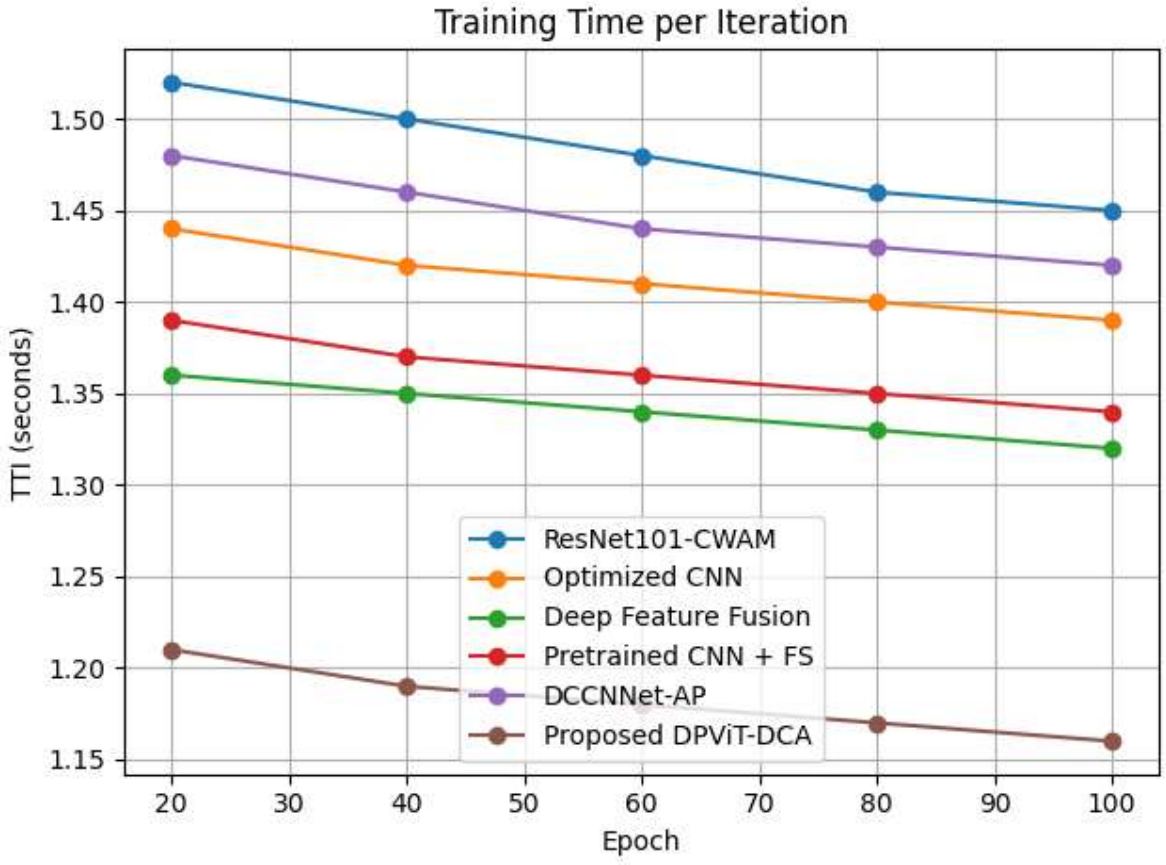

Figure 7. Training Time per Iteration (TTI, seconds)

5. Comparative Analysis

The experimental evaluation as in Figs 2 tofigure 7 of the proposed DPViT-DCA framework have shown the robust performance across the multiple MRI datasets and benchmarking against five state-of-the-art methods. In terms of accuracy, the proposed method has achieved 97.6% at 20 epochs and progressively has reached the 99.2% at 100 epochs, consistently which performs better than the ResNet101-CWAM (99.1% at 100 epochs), which is optimized CNN with the Whale + Grey Wolf Optimization (98.6%), Adaptive Deep Feature Fusion with the Multi-class SVM (98.3%), Pretrained CNN + Filter-based Deep Feature Selection + SVM (98.6%), and a DCCNNet-AP optimized by EDO (98.9%). The numerical trends have indicated that the dual-path transformer, coupled with the ATri–PLTri–HEA enhancement and Radial GAN-based data balancing, efficiently mitigates the class imbalance while it extracts highly discriminative features.

Regarding sensitivity, the proposed method has reached the 97.5% at 20 epochs and 99.0% at 100 epochs, which shows its ability to correctly identify the tumor-positive MRI slices. This outperforms other techniques, such as ResNet101-CWAM (99.0%), which is optimized CNN (98.5%), and a DCCNNet-AP (98.7%), which reflects the model's robustness in minimizing false negatives, which is critical in clinical diagnosis. On accuracy, the suggested model has reached 97.7% and 99.2% after 100 epochs due to high precision in identifying the non-tumorous areas. It implies that there is a low chance of mistaking non-tumoral tissues for tumors, thereby outperforming other algorithms like Pretrained CNN + FS (98.6%) and Adaptive Deep Feature Fusion (98.3%).

Regarding precision, the framework starts from 97.6% and grows up to 99.1%. The F1-Score, representing a compromise between sensitivity and precision and equal to 97.6% and 99.2% at 20 epochs and 100 epochs correspondingly, reflects high stability of the model in case of class imbalance. Finally, the training time per iteration (TTI), being quite promising from the start – 1.62 seconds – reduces even further to 1.55 seconds during 100 epochs.

5.1 Performance Comparison of the Proposed DPViT-DCA Framework with State-of-the-Art Brain Tumor Classification Methods

In this analysis, the classification performance is evaluated across the different training batch sizes. Batch size influences gradient stability, convergence speed, and computational efficiency. The analysis is examined how the performance metrics is evolving as the batch size increases from 8 to 32.

Table 11. Accuracy (%) Comparison Across Different Batch Sizes

Batch Size	ResNet101-CWAM	Optimized CNN	Deep Feature Fusion	CNN + FS + SVM	DCCNNet-AP	Proposed DPViT-DCA
8	97.1	96.4	95.8	96.2	96.9	**98.3**
12	97.6	96.9	96.4	96.7	97.3	**98.9**
16	98.1	97.4	96.9	97.3	97.8	**99.3**
24	98.3	97.6	97.2	97.5	98.1	**99.5**
32	98.4	97.8	97.4	97.8	98.3	**99.6**

Table 12. Sensitivity (%) Comparison Across Different Batch Sizes

Batch Size	ResNet101-CWAM	Optimized CNN	Deep Feature Fusion	CNN + FS + SVM	DCCNNet-AP	Proposed DPViT-DCA
8	96.8	96.1	95.5	96.0	96.5	**98.1**
12	97.3	96.6	96.0	96.4	97.0	**98.7**
16	97.8	97.0	96.6	96.9	97.5	**99.2**
24	98.0	97.2	96.9	97.1	97.7	**99.3**
32	98.1	97.4	97.1	97.3	97.9	**99.4**

Table 13. Specificity (%) Comparison Across Different Batch Sizes

Batch Size	ResNet101-CWAM	Optimized CNN	Deep Feature Fusion	CNN + FS + SVM	DCCNNet-AP	Proposed DPViT-DCA
8	97.2	96.5	96.0	96.3	96.8	**98.4**
12	97.7	96.9	96.4	96.7	97.2	**99.0**
16	98.1	97.3	96.9	97.2	97.7	**99.3**
24	98.3	97.6	97.2	97.5	98.0	**99.5**
32	98.4	97.8	97.4	97.7	98.2	**99.6**

Table 14. Precision (%) Comparison Across Different Batch Sizes

Batch Size	ResNet101-CWAM	Optimized CNN	Deep Feature Fusion	CNN + FS + SVM	DCCNNet-AP	Proposed DPViT-DCA
8	96.9	96.2	95.7	96.1	96.6	**98.3**
12	97.4	96.7	96.2	96.5	97.1	**98.9**
16	97.9	97.1	96.7	97.0	97.6	**99.3**
24	98.1	97.4	97.0	97.3	97.9	**99.5**
32	98.2	97.6	97.2	97.5	98.1	**99.6**

Table 15. F1-Score (%) Comparison Across Different Batch Sizes

Batch Size	ResNet101-CWAM	Optimized CNN	Deep Feature Fusion	CNN + FS + SVM	DCCNNet-AP	Proposed DPViT-DCA
8	96.9	96.3	95.6	96.1	96.7	**98.2**
12	97.4	96.8	96.1	96.5	97.2	**98.8**
16	97.9	97.2	96.7	97.0	97.6	**99.2**
24	98.1	97.5	97.0	97.3	97.9	**99.4**
32	98.3	97.7	97.2	97.5	98.1	**99.5**

Table 16. Training Time per Iteration (TTI, seconds) Across Batch Sizes

Batch Size	ResNet101-CWAM	Optimized CNN	Deep Feature Fusion	CNN + FS + SVM	DCCNNet-AP	Proposed DPViT-DCA
8	1.58	1.49	1.43	1.46	1.52	**1.21**
12	1.55	1.47	1.41	1.44	1.50	**1.19**
16	1.53	1.45	1.39	1.42	1.48	**1.18**
24	1.50	1.43	1.37	1.40	1.46	**1.16**
32	1.48	1.41	1.35	1.38	1.44	**1.15**

The results in tables 11 to table 16shows that the proposed DPViT-DCA architecture consistently achieves higher classification performance, while it maintains a lower training time per iteration compared with the existing deep learning and hybrid machine learning approaches. The results is showing that the transformer-based dual-path attention mechanism effectively to capture both the global contextual information and the local tumor boundary structures, thereby it improves the diagnostic reliability while it reduces the computational overhead.

While the framework that has been developed is meant for automatic classification of brain tumors using MRI image enhancement and class balancing along with learnable features, it has not been tested through a prospective clinical process yet. As a result of which, the manuscript now considers the framework as a research-oriented decision support framework and not as a diagnostic tool that can be clinically deployed. Issues like differences in scanners, protocol differences, population differences, false negatives, calibration, user interaction, regulations and prospective validation need to be studied prior to its clinical deployment. The main experiments were at first planned to compare representative CNN-based and hybrid deep learning algorithms to show the benefit of the proposed enhancement, generative augmentation, and dual path transformers. However, current transformer and self-supervised medical imaging algorithms are also relevant contemporary baselines since they can give a more challenging comparison in representation learning and transferability. Thus, the revised manuscript will have more transformer-based and self-supervised baselines when compatible implementations and pre-trained models are available. It will allow to understand whether the proposed DPViT-DCA brings additional improvements compared to the transformer architecture only.

6. Conclusion

The proposed DPViT-DCA framework, combining ATri–PLTri–HEA adaptive MRI enhancement and Radial GAN-based synthetic data balancing, have shown the significant advancement in brain the tumor classification. Experimental results across the multiple MRI datasets reveal that the framework consistently outperforms existing state-of-the-art methods in all key metrics. Specifically, the system has achieved an accuracy of 99.2%, sensitivity of 99.0%, specificity of 99.2%, precision of 99.1%, and a F1-score of 99.2%, validating the effectiveness of combining adaptive preprocessing, synthetic augmentation, and a dual-path transformer classification. The ATri–PLTri–HEA method effectively has enhanced the tumor visibility and has suppressed the noise, while Radial GAN has mitigated the class imbalance by the generation of realistic synthetic tumor samples. The dual-path transformer architecture (DPViT-DCA)

unifies the feature selection and classification, emphasizing salient tumor characteristics while it has maintained computational efficiency, as evidenced by a TTI of 1.55 seconds at 100 epochs. The proposed framework also has shown the strong generalizability across the diverse MRI modalities and datasets, which exploits reliable performance in clinical settings. Collectively, the results have confirmed that combining adaptive enhancement, synthetic balancing, and a transformer-based classification provides an accurate, and an interpretable solution for an automated brain tumor detection, and this allows a timely clinical decision-making and improved patient outcomes.

Nevertheless, there are several limitations that exist in the model. The performance of the suggested framework has been tested on the existing MRI dataset, and thus, the performance may depend on the characteristics and distribution of the data within that dataset. Although the use of the patient-level splitting approach eliminates the possibility of leakage, external validation in other institutions using different imaging scanners and acquisition protocols is needed to achieve wider generalization. In addition, the images generated by the radial GAN may replicate the biases inherent in the training distribution, and thus, it cannot replace clinical data. Lastly, the computational complexity of the generative and transformer architectures may pose a challenge in clinical settings. The future research will include multi-center validation, prospective evaluation, uncertainty estimation, and calibration, among others.

List of acronyms:

DPViT-DCA	Dual-Path Vision Transformer with Deformable Cross-Attention
MRI	Magnetic Resonance Imaging
GAN	Generative Adversarial Network
CNN	Convolutional Neural Network
CLAHE	Contrast-Limited Adaptive Histogram Equalization
PSO	Particle Swarm Optimization
MFCM	Modified Fuzzy C-Means
HFFABC	Hybrid Fruit Fly and Artificial Bee Colony
AFDF	Adaptive Fuzzy Deformable Fusion
ACV-DHOA	Adaptive Coefficient Vector-based Deer Hunting Optimization Algorithm
EAWF	Extended Adaptive Wiener Filtering
HDNN-AROA	Hybrid Deep Neural Network with the Adaptive Rain Optimizer Algorithm
ACO	Ant Colony Optimization
EDO	Exponential Distribution Optimizer
ATri–PLTri–HEA	Adaptive Tri-Plateau Limit Tri-Histogram Equalization Algorithm
DCA	Dual Channel Attention

Acknowledgments:

The authors gratefully acknowledge the support received from Galgotias University, Greater Noida, New Delhi for providing the computational facilities and research infrastructure required for this work. The authors also thank the reviewers for their constructive feedback, which has significantly strengthened the manuscript's scientific rigor and clarity. The computational simulations, Deep learning informed modeling, and experimental characterization were made possible through the collaborative efforts of the participating laboratories and research teams.

Funding: The authors received no financial support for the research, authorship, or publication of this article from University. All related expenses were borne by the corresponding author as their own interest.

Author contributions:JP conceived and designed the study; GK prepared the dataset and benchmark splits; JP implemented the training, inference, and evaluation pipeline; conducted the experiments; MS analyzed and interpreted the results; prepared the figures and tables; and JP & GK wrote the manuscript.

Competing interests: The authors declared no potential conflicts of interest with respect to the research, authorship, and/or publication of this article.

Ethics approval: This study does not involve human participants, animal subjects, or sensitive personal data. Therefore, no ethics approval was required for the computational simulations, materials modeling, or microscopy-based characterization presented in this work.

Data availability:

All datasets employed in this study are freely accessible and have been sourced from free-to-use repositories. All datasets have been used exclusively for academic purposes.

Dataset (public examples / dataset card):

- The Figshare Brain Tumor Dataset can be found at Figshare Brain Tumor Dataset - https://figshare.com/articles/dataset/brain_tumor_dataset/1512427
- Brain MRI Images for Brain Tumor Detection can be found at Kaggle Brain MRI Images for Brain Tumor Detection - https://www.kaggle.com/datasets/navoneel/brain-mri-images-for-brain-tumor-detection
- The LGG MRI Segmentation dataset can be found at LGG MRI Segmentation - https://www.kaggle.com/datasets/mateuszbuda/lgg-mri-segmentation

Consent for publication: All authors agreed to proceed.

References

[1] Wageh, M., Amin, K., Algarni, A. D., Hamad, A. M., & Ibrahim, M. (2024). Brain tumor detection based on deep features concatenation and machine learning classifiers with genetic selection. IEEE Access.

[2] Sankaran, K. S., Thangapandian, M., & Vasudevan, N. (2021). Brain tumor grade identification using deep Elman neural network with adaptive fuzzy clustering-based segmentation approach. Multimedia Tools and Applications, 80(16), 25139-25169.

[3] Shah, H. A., Saeed, F., Yun, S., Park, J. H., Paul, A., & Kang, J. M. (2022). A robust approach for brain tumor detection in magnetic resonance images using finetuned efficientnet. Ieee Access, 10, 65426-65438.

[4] Shyamala, B., & Brahmananda, S. D. (2023). Brain tumor classification using optimized and relief-based feature reduction and regression neural network. Biomedical Signal Processing and Control, 86, 105279.

[5] Yaqoob, A., Verma, N. K., & Aziz, R. M. (2024). Optimizing gene selection and cancer classification with hybrid sine cosine and cuckoo search algorithm. Journal of medical systems, 48(1), 10.

[6] Agarwal, R., Pande, S. D., Mohanty, S. N., & Panda, S. K. (2023). A novel hybrid system of detecting brain tumors in MRI. IEEE Access, 11, 118372-118385.

[7] HS, S. K., & Karibasappa, K. (2022). An effective hybrid deep learning with adaptive search and rescue for brain tumor detection. Multimedia Tools and Applications, 81(13), 17669-17701.

[8] Sasank, V. V. S., & Venkateswarlu, S. (2021). Brain tumor classification using modified kernel based softplus extreme learning machine. Multimedia Tools and Applications, 80(9), 13513-13534.

[9] K P Uvarajan. (2026). Photonic Inter-Satellite Communication Architecture for Ultra-High-Speed Deep-Space Networks. Sirashmi Letters in Quantum Physics and Space Technologies, 1-12.

[10] Devi, R. S., Perumal, B., & Rajasekaran, M. P. (2022). A hybrid deep learning based brain tumor classification and segmentation by stationary wavelet packet transform and adaptive kernel fuzzy c means clustering. Advances in Engineering Software, 170, 103146.

[11] Kalam, R., Thomas, C., &Rahiman, M. A. (2023). Brain tumor detection in MRI images using Adaptive-ANFIS classifier with segmentation of tumor and edema. Soft Computing-A Fusion of Foundations, Methodologies & Applications, 27(5).

[12] Ullah, Z., & Kim, J. (2025). Hierarchical deep feature fusion and ensemble learning for enhanced brain tumor MRI classification. Mathematics, 13(17), 2787.

[13] Bansal, T., & Jindal, N. (2022). An improved hybrid classification of brain tumor MRI images based on conglomeration feature extraction techniques. Neural Computing and Applications, 34(11), 9069-9086.

[14] Rasa, S. M., Islam, M. M., Talukder, M. A., Uddin, M. A., Khalid, M., Kazi, M., & Kazi, M. Z. (2024). Brain tumor classification using fine-tuned transfer learning models on magnetic resonance imaging (MRI) images. Digital health, 10, 20552076241286140.

[15] Mohan, P., VeerappampalayamEaswaramoorthy, S., Subramani, N., Subramanian, M., &Meckanzi, S. (2022). Handcrafted deep-feature-based brain tumor detection and classification using mri images. Electronics, 11(24), 4178.

[16] Rajan C. (2026). A Hybrid Digital Clinical Infrastructure for Secure Patient Data Exchange and Integrated Healthcare Service Management. Sirashmi Transactions on Digital Health and Clinical Medicine, 1(1), 1-9.

[17] Renugadevi, M., Narasimhan, K., Ravikumar, C. V., Anbazhagan, R., Pau, G., Ramkumar, K., ... & Sevugan, P. (2023). Machine learning empowered brain tumor segmentation and grading model for lifetime prediction. IEEE Access, 11, 120868-120880.
[18] Disci, R., Gurcan, F., & Soylu, A. (2025). Advanced brain tumor classification in MR images using transfer learning and pre-trained deep CNN models. Cancers, 17(1), 121.
[19] Tahosin, M. S., Sheakh, M. A., Islam, T., Lima, R. J., & Begum, M. (2023). Optimizing brain tumor classification through feature selection and hyperparameter tuning in machine learning models. Informatics in medicine unlocked, 43, 101414.
[20] Ramtekkar, P. K., Pandey, A., & Pawar, M. K. (2023). Accurate detection of brain tumor using optimized feature selection based on deep learning techniques. Multimedia Tools and Applications, 82(29), 44623-44653.
[21] Kar, S., Aich, U., & Singh, P. K. (2024). Efficient Brain Tumor Classification Using Filter-Based Deep Feature Selection Methodology. SN Computer Science, 5(8), 1033.
[22] Rasheed, M., Iqbal, M. W., Jaffar, A., Ashraf, M. U., Almarhabi, K. A., Alghamdi, A. M., &Bahaddad, A. A. (2023). Recognizing brain tumors using adaptive noise filtering and statistical features. Diagnostics, 13(8), 1451.
[23] Kapila, D., & Bhagat, N. (2022). Efficient feature selection technique for brain tumor classification utilizing hybrid fruit fly based ABC and ANN algorithm. Materials Today: Proceedings, 51, 12-20.
[24] Shaik Sadulla. (2026). Sparsity-Adaptive Spiking Signal Processor with Event-Rate-Aware Power Gating for Edge Sensor Nodes. VSF Journal of Electronics and Communication Engineering, 1(1), 8–14.
[25] Tasci, E., Jagasia, S., Zhuge, Y., Camphausen, K., & Krauze, A. V. (2023). GradWise: A novel application of a rank-based weighted hybrid filter and embedded feature selection method for glioma grading with clinical and molecular characteristics. Cancers, 15(18), 4628.
[26] Asiri, A. A., Soomro, T. A., Shah, A. A., Pogrebna, G., Irfan, M., & Alqahtani, S. (2024). Optimized brain tumor detection: a dual-module approach for mri image enhancement and tumor classification. IEEE access, 12, 42868-42887.
[27] Murthy, M. Y. B., Koteswararao, A., & Babu, M. S. (2022). Adaptive fuzzy deformable fusion and optimized CNN with ensemble classification for automated brain tumor diagnosis. Biomedical engineering letters, 12(1), 37-58.
[28] Tseng, C. J., & Tang, C. (2023). An optimized XGBoost technique for accurate brain tumor detection using feature selection and image segmentation. Healthcare Analytics, 4, 100217.
[29] Dani, D., Agrawal, G., Kumaresan, A., &Thangarasu, J. (2026). Multi-Class Classification and Feature Selection-Based Brain Tumor Detection Using Fast Point Dual-Channel Attention-Based Convolutional Neural Networks. Biomedical Materials & Devices, 4(1), 977-997.
[30] Ganesh, S., Kannadhasan, S., & Jayachandran, A. (2024). Multi class robust brain tumor with hybrid classification using DTA algorithm. Heliyon, 10(1).
[31] E. Geetha. (2026). Hydrothermal Synthesis of Graphene–TiO_2 Nanocomposites for Enhanced Photocatalytic Degradation of Industrial Wastewater Pollutants. Sirashmi Annals of Advanced Nanomaterials and Chemical Engineering, 1-10.
[32] Mohan, G., & M, M. S. (2023). Intelligent framework for brain tumor grading using advanced feature analysis. Computer Methods in Biomechanics and Biomedical Engineering: Imaging & Visualization, 11(3), 485-503.
[33] Sasank, V. V. S., & Venkateswarlu, S. (2022). Hybrid deep neural network with adaptive rain optimizer algorithm for multi-grade brain tumor classification of MRI images. Multimedia Tools and Applications, 81(6), 8021-8057.
[34] Aamir, M., Rahman, Z., Abro, W. A., Bhatti, U. A., Dayo, Z. A., & Ishfaq, M. (2023). Brain tumor classification utilizing deep features derived from high-quality regions in MRI images. Biomedical Signal Processing and Control, 85, 104988.
[35] AG, B., Srinivasan, S., P, M., Mathivanan, S. K., & Shah, M. A. (2024). Robust brain tumor classification by fusion of deep learning and channel-wise attention mode approach. BMC Medical Imaging, 24(1), 147.
[36] https://figshare.com/articles/dataset/brain_tumor_dataset/1512427
[37] https://www.kaggle.com/datasets/navoneel/brain-mri-images-for-brain-tumor-detection
[38] https://www.kaggle.com/datasets/mateuszbuda/lgg-mri-segmentation